High-resolution time–frequency distributions for manoeuvring target detection in over-the-horizon radars

Y. Zhang, M.G. Amin and G.J. Frazer

Abstract: A novel high-resolution time–frequency representation method is proposed for source detection and classification in over-the-horizon radar (OTHR) systems. A data-dependent kernel is applied in the ambiguity domain to capture the target signal components, which are then resolved using root-MUSIC based coherent spectrum estimation. This two-step procedure is particularly effective for analysing a multicomponent signal with time-varying complex time–Doppler signatures. By using the different time–Doppler signatures, important target manoeuvring information, which is difficult to extract using other linear and bilinear time–frequency representation methods, can be easily revealed using the proposed method.

1 Introduction

By exploiting the reflective and refractive nature of high-frequency (HF) radiowave propagation through the ionosphere, over-the-horizon radars (OTHRs) perform wide-area surveillance at long range well beyond the limit of the horizon of conventional line-of-sight (LOS) radars. OTHR systems have become an important tool for wide-area surveillance [1–5].

A significant problem in OTHR is robust high-resolution Doppler processing of accelerating or decelerating targets. This arises during aircraft and ship target manoeuvre and during observations of rockets during the boost phase and in mid-course flight. The complex Doppler signatures present in these cases reveal important information about the target.

Most OTHR systems use classical Doppler processing, where one Doppler spectrum is computed using one full coherent integration time (CIT, typically 1–100 s in OTHR). Some systems use overlapped Doppler processing to provide a spectrogram analysis of time-varying Doppler. Accelerating/decelerating targets smear in Doppler and have reduced detectability and localisation. The smearing reduces resolution and can obscure important multicomponent Doppler features.

There are numerous time–frequency distributions (TFDs) other than the spectrogram [6–8]. Many TFDs provide superior localisation in time and Doppler frequency. Previous applications of time–frequency signal representations to OTHR, however, have generally been disappointing. The fundamental challenge with OTHR is that the TFD must retain its desirable resolution and concentration properties in the presence of clutter that is typically 40 dB or more stronger than the target (although possibly localised in a different region of time–Doppler).

The objective of this paper is to investigate and extend recent developments in data-dependent TFDs to the problem of robust high-resolution analysis of time-varying OTHR target returns. Of particular interest is the problem of multicomponent target signal detection and identification, where important information concerning the manoeuvring target can be revealed. Such information is significant for the classification of manoeuvring targets.

2 Signal model

2.1 Signal model

Figure 1*a* illustrates a stylised OTHR system. For simplicity of mathematical analysis, we adopt the flat ground model, as shown in Fig. 1*b*.

The received signal, after pulse or sweep matched filtering and beamforming at the receiver, is expressed as

$$y(t) = x(t) + u(t) + n(t) \tag{1}$$

where $u(t)$ is the clutter, and $x(t)$ is the return signal from the target, expressed as

$$x(t) = Ae^{-j\omega_c(d_t+d_r)/c} \tag{2}$$

where A is a complex scalar representing the propagation loss and phase, d_t and d_r are the respective one-way slant range between the transmitter and the target and between the target and the receiver, c denotes the speed of light and $\omega_c = 2\pi f_c$ is the carrier radian frequency. In (1), $n(t)$ is internal and external noise, whose power is small in a typical situation with strong target signal-to-noise ratio. Therefore, the noise term is ignored in this paper.

In a typical OTHR scenario, as shown in Fig. 1*a*, in addition to the path directly reflected from the ionosphere, there is reflection at the ground near the target. Denote l_1 and l_2 as the propagation distance of the two paths, respectively, and d_t and d_r as the respective one-way slant range between the transmitter and the target and between the target and the receiver, respectively. Then, d_t takes the value

IEE Proceedings online no. 20030672

doi: 10.1049/ip-rsn:20030672

Paper first received 18th December 2002 and in revised form 27th May 2003

Y. Zhang and M.G. Amin are with the Center for Advanced Communications, Villanova University, Villanova, PA 19085, USA

G.J. Frazer is with the ISR Division, DSTO, Edinburgh, Australia

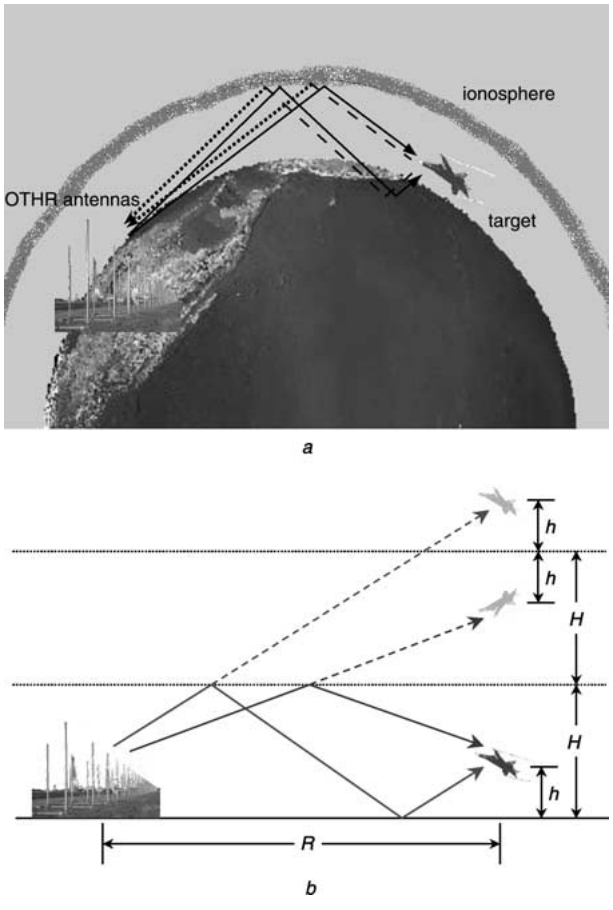

Fig. 1 *OTHR system and flat ground model*
a OTHR system
b Flat ground approximation

of either l_1 and l_2 and so does d_r. (Some OTHR systems are bistatic in which case the transmitter and receiver are in different locations. In this case, the range from the target to the transmitter and that from the target to the receiver are different. We have ignored this difference, however, as it does not significantly affect our results.) The corresponding path losses will be denoted as A_1 and A_2. Therefore, the received signal consists of four combination paths which result in the following three multipath components:

$$x(t) = A_1 e^{-j\omega_c 2l_1/c} + A_2 e^{-j\omega_c 2l_2/c} + A_3 e^{-j\omega_c (l_1+l_2)/c} \quad (3)$$

We will refer to the path $(l_1 : l_1)$ as path I, path $(l_2 : l_2)$ as path II, and the combination of path $(l_1 : l_2)$ and $(l_2 : l_1)$ as path III.

Based on the flat ground model approximation illustrated in Fig. 1*b*, the slant ranges l_1 and l_2, respectively, can be expressed in terms of the range distance R, the ionosphere height H and the aircraft height h, as

$$l_1 = (R^2 + (2H - h)^2)^{1/2}, \quad l_2 = (R^2 + (2H + h)^2)^{1/2} \quad (4)$$

To clearly reveal the relationship between the slant ranges and the parameters, we take into account the fact that $R \gg H \gg h$ hold for a typical scenario. Then, the above expressions can be approximated as

$$l_1 \approx R + \frac{2H^2 - 2Hh}{R}, \quad l_2 \approx R + \frac{2H^2 + 2Hh}{R} \quad (5)$$

2.2 Doppler characteristics

The flight of an aircraft, in general, consists of horizontal and elevation movements. In this Section, we consider the Doppler frequency characteristics of the aircraft's movement in the two different dimensions.

As an aircraft flies, R, and possibly also h, become functions of t. The height of the ionosphere H is also slowly time-varying. However, we assume that H is a constant over the processing time interval. From (5), we obtain

$$\frac{dl_1(t)}{dt} \approx K(t)v_R(t) - \frac{2H}{R(t)}v_c(t),$$
$$\frac{dl_2(t)}{dt} \approx K(t)v_R(t) + \frac{2H}{R(t)}v_c(t) \quad (6)$$

where $K(t) = (1 - 2H^2/R^2(t))$, $v_R(t) = dR(t)/dt$ is the target velocity in the range direction toward the radar and $v_c(t) = dh(t)/dt$ is the ascending velocity of the target. The Doppler frequencies of the three different paths are then obtained as

$$f_I(t) = \frac{2f_c}{c}\frac{dl_1(t)}{dt} \approx \frac{2f_c}{c}K(t)v_R(t) - \frac{4f_cH}{R(t)c}v_c(t)$$
$$f_{II}(t) = \frac{2f_c}{c}\frac{dl_2(t)}{dt} \approx \frac{2f_c}{c}K(t)v_R(t) + \frac{4f_cH}{R(t)c}v_c(t)$$
$$f_{III}(t) = \frac{f_c}{c}\frac{dl_1(t) + dl_2(t)}{dt} \approx \frac{2f_c}{c}K(t)v_R(t) \quad (7)$$

From the above discussion, it is evident that, while the dominant Doppler component $2f_cK(t)v_R(t)/c$ is shared by all three paths and reveals the target velocity in the range direction, the small Doppler difference between the paths is a function of $h(t)$ and, therefore, reveals other important information on how the target moves in the elevation direction.

In this paper, we consider an often encountered scenario of a manoeuvring aircraft as an example. In this case, the target makes a 180° turn in $T = 30.72$ s to change height and direction. This time interval corresponds to six revisits (blocks), and each block contains 256 samples (slow time samples from the radar). The parameters used in the analysis and simulations are listed in Table 1. All the multipath signals are considered to fall within the same range cell.

The range is expressed as

$$R(t) = R(0) - \frac{v_R(t)T}{\pi}\sin\left(\frac{t\pi}{T}\right) \quad (8)$$

and the height is expressed as

$$h(t) = h(0) + \frac{v_c(t)T}{\pi}\left[1 - \cos\left(\frac{t\pi}{T}\right)\right] \quad (9)$$

The cross-range movement is not considered because it does not significantly contribute to the Doppler frequency. Substituting (8) and (9) into (5) yields the following

Table 1: Major parameters

Parameter	Notation	Value
Initial range	$R(0)$	2000 km
Ionosphere height	H	350 km
Aircraft initial height	$h(0)$	10000 m
Maximum range speed	v_R	500 km/h
Maximum climbing speed	v_c	1500 m/min
Carrier frequency	f_c	20 MHz
Waveform repetition frequency	f_s	50 Hz
Samples per block	N	256 samples

Doppler frequency:

$$f(t) = f_R(t) + f_h(t) \tag{10}$$

where $f_R(t)$ is the Doppler frequency caused by the change of $R(t)$ and is expressed as

$$f_R(t) = \frac{2f_c}{c} v_R(t) = \frac{2vf_c}{c} \cos\left(\frac{t - t_1}{T}\pi\right) \tag{11}$$

and $f_h(t)$ in (10) is the Doppler frequency caused by the change of height $h(t)$ and is expressed, for path I, as

$$f_{h,I}(t) = \frac{4v_c(t)f_c H}{R(t)c} \sin\left(\frac{t - t_1}{T}\pi\right) \tag{12}$$

It is easy to confirm that $f_{h,II}(t) = -f_{h,I}(t)$ and $f_{h,III}(t) = 0$ for all t.

The time–Doppler signatures are plotted in Fig. 2. The dominant Doppler component is proportional to the target velocity in the slant range direction, and the small Doppler difference between the three paths is proportional to the ascending velocity of the target. This difference provides important information on how the target moves in the elevation direction. The maximum one-side Doppler difference corresponding to the maximum ascending speed 1500 m/ min = 25 m/s is about 1.17 Hz.

The frequency resolution in the underlying system is $\Delta f = f_s/N = 50/256 = 0.195$ Hz. The detection of such a small Doppler difference is possible through the application of discrete Fourier transform (DFT) to the received signal, provided that $v(t)$ and, subsequently, $2f_c v(t)/c$ are fixed over the CIT of 256 samples. However, when v_R is not a constant, which occurs if the target is accelerating or decelerating, ascending or descending, or, changing its direction, $2f_c v(t)/c$ becomes time-varying and the conventional DFT-based approach does not provide high Doppler resolution even with a long CIT [9]. In this case, the detection and estimation of the Doppler shift caused by a change of h become difficult. The presence of strong clutter adds more difficulties to the underlying problem.

Conventional methods based on spectrogram and other TFDs smear the target's Doppler signature and cannot provide satisfactory resolution performance. The smearing reduces resolution and is likely to obscure important multicomponent time–Doppler signatures. To realise high-resolution Doppler detection and estimation, we must first proceed with clutter suppression followed by an effective time–Doppler processing method. The combination of the two methods clearly reveals the interested time–Doppler signatures.

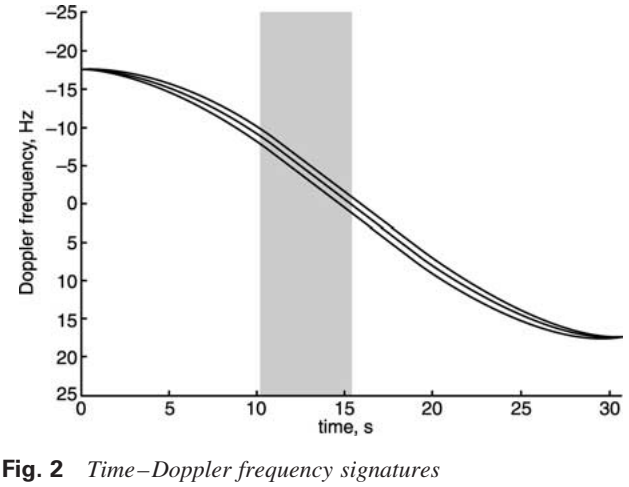

Fig. 2 *Time–Doppler frequency signatures*

3 Clutter suppression

We consider TFD methods to achieve high-resolution time–Doppler localisation. In the underlying problem, TFDs are referred to as time–Doppler distributions (TDDs). The most commonly used TFD is the Wigner–Ville distribution (WVD). The WVD of signal $y(t)$ is defined as

$$W_{yy}(t,f) = \int y(t + \tau/2)y^*(t - \tau/2)e^{-j\omega\tau}d\tau \tag{13}$$

where the superscript '$*$' denotes complex conjugate. All integrals without limits imply integration from $-\infty$ to $+\infty$. Substituting (1) in (13), the WVD of $y(t)$ can be written in terms of

$$W_{yy}(t,f) = W_{xx}(t,f) + W_{uu}(t,f) + W_{xu}(t,f) + W_{ux}(t,f) \tag{14}$$

where the first two terms are, respectively, the autoterms of the target signal and the clutter, and the other two are their cross-terms.

In a typical OTHR receiver, the clutter is much stronger (typically 30–50 dB) than the target signal. Without substantial suppression of the clutter, the TDD autoterm of the target will be significantly obscured by the clutter autoterm as well as the cross-terms between the clutter and signal.

Clutter often has high correlation to that at its neighbouring range cells and cross-range cells. Based on this property, clutter mitigation methods using received signals from other range and cross-range cells have been proposed in, for example, [9, 10]. However, in this paper, the received signal from other range and cross-range cells are not used.

We point to the fact that the clutter is highly localised in low frequencies and can be well modelled as an auto-regressive (AR) process [11, 12]. Therefore, the clutter can be substantially suppressed by using the AR pre-whitening techniques. Denote P as the order of the AR model, the AR polynomial parameters $a(t)$, $t = 0, \ldots, P$ can be estimated via the modified covariance method [13].

Filtering the received signal $y(t)$ through a finite impulse filter (FIR), constructed using the AR polynomial parameters, results in the pre-whitened signal

$$z(t) = y(t) * a(t) = x(t) * a(t) + u(t) * a(t) \triangleq z_x(t) + z_u(t) \tag{15}$$

where '$*$' denotes the convolution operator.

In this paper, the target signal calculated in Section 2 is overlaid to real OTHR clutter data. We assume that $A_1 = A_2$ and $A_3 = A_1 + A_2 = 2A_1$. The order of the AR model should be chosen to maximise the signal-to-clutter ratio (SCR). The order of the AR model is set to a unit value ($P = 1$). The spectrogram of block 3, which corresponds to the 256 samples from 10.24 to 15.36 seconds, before and after the AR pre-whitening is shown in Fig. 3. It is seen that, while the clutter is substantially suppressed by more than 40 dB, the target signal is only partially affected when its Doppler frequency is very close to that of the clutter. Figures 4 and 5 show the WVDs of the $y(t)$ and $z(t)$ before and after the pre-whitening. The WVDs are computed from the interpolated data sequence to show the full Doppler-frequency range. While it is often difficult to identify the target in the WVD before pre-whitening (Fig. 4), the target signature can now be somewhat identified in Fig. 5. Further

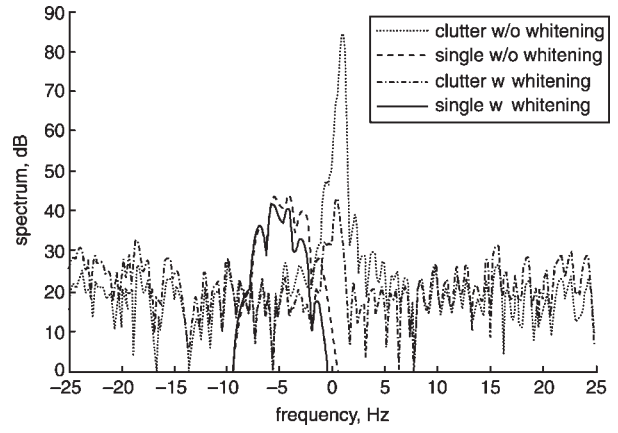

Fig. 3 *Block-wise spectrogram of the received signal before and after AR pre-whitening*

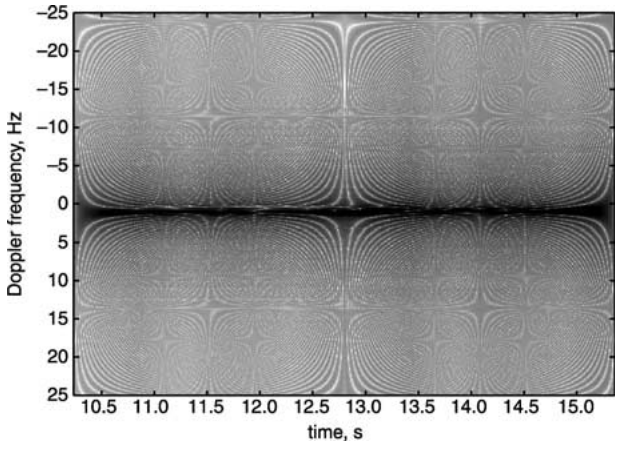

Fig. 4 *WVD of received signal y(t) before AR pre-whitening (block 3)*

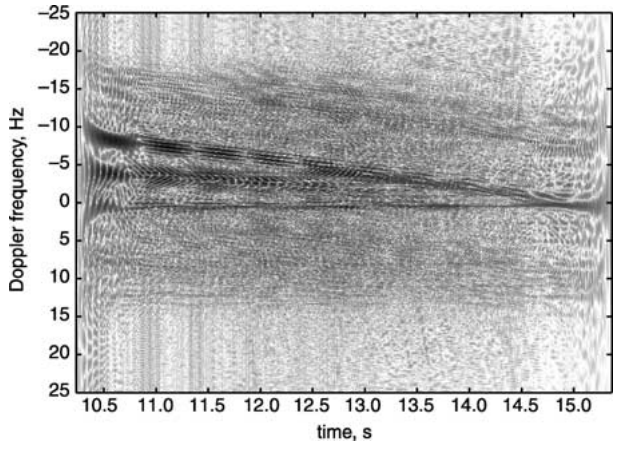

Fig. 5 *WVD of the received signal z(t) after AR pre-whitening (block 3)*

and key improvement in resolutions of the target signature components can be achieved by using the techniques highlighted in Section 4.

4 High-resolution time–Doppler processing

Even after substantial clutter suppression, the result in Fig. 5 does not reveal clear time–Doppler signatures. There are numerous TFDs other than the spectrogram and the WVD which provide superior localisation. Previous applications of time–frequency signal representation techniques to the OTHR problem, however, have generally been disappointing because the problem is particularly difficult and demanding.

To achieve chirp signal detection, discrimination and classification, we propose time–Doppler estimation based on adaptive kernel and high-resolution time–Doppler localisation. Bilinear TDDs as well as their Fourier transforms (i.e. ambiguity functions and local autocorrelation functions) are considered.

4.1 Time–Doppler distributions and adaptive kernel

In the following, we assume that each component of the return signal from the target can be approximated as a chirp over the period of one block, i.e.

$$x(t) = \sum_{i=1}^{3} A_i e^{j(\alpha_i t + \beta_x t^2/2)} \tag{16}$$

is considered for a time period. Such approximation permits us to obtain important signal information, as discussed in Section 2, from the received data signal.

To estimate the chirp rate of the signal, it is common to examine the ambiguity function. The ambiguity function of $z(t)$ is defined as

$$A_z(\theta, \tau) = \int_t z(t + \tau/2) z^*(t - \tau/2) e^{j\theta t} dt \tag{17}$$

where θ and τ are, respectively, the frequency-lag and time-lag variables. Similar to the TDD, the ambiguity function can be decomposed into two autoterms and two cross-terms. One important property of the ambiguity function is that all signal autoterms pass through the origin, whereas the cross-terms are often away from the origin. For a multicomponent parallel chirp signal, the ambiguity function shows linear signatures depending on the signal chirp rate. Therefore, unlike the time–Doppler domain, in which a two-dimensional search is required, the chirp rate in the ambiguity domain can be estimated by a one-dimensional search. The reduction in computations make the ambiguity domain attractive for chirp rate estimation.

The chirp rate can be estimated by searching for the peaks of the following Q function [14]:

$$Q(\xi) = \int |A_z(r \cos \xi, r \sin \xi)| dr \tag{18}$$

In the case considered, peaks possibly appear at $\xi_x = -1/\tan^{-1}(\beta_x)$ and $\xi_u = -1/\tan^{-1}(\beta_u)$, were β_x and β_u are the chirp rates of the signal and the principal component of the residual clutter, respectively. The Q function calculated for block 3 is shown in Fig. 6.

Based on the chirp rate estimation, an adaptive kernel can be designed. We construct a kernel whose passband only captures the target signal chirp rate. The clutter will be, subsequently, mitigated in the ambiguity domain due to its distinct orientation compared to the target signal. For an estimated chirp rate $\hat{\xi}_x$, the following adaptive kernel is constructed to encompass the autoterm ambiguity function of the target signal, i.e.

$$\phi_a(\theta, \tau) = e^{-d^2(\theta,\tau)/\sigma^2} \tag{19}$$

where σ is the kernel width, and

$$d^2(\theta, \tau) = \theta^2 + \tau^2 - (\theta \sin \hat{\xi}_x + \tau \cos \hat{\xi}_x)^2 \tag{20}$$

The adaptive kernel suppresses the clutter and noise, as well as all cross-terms.

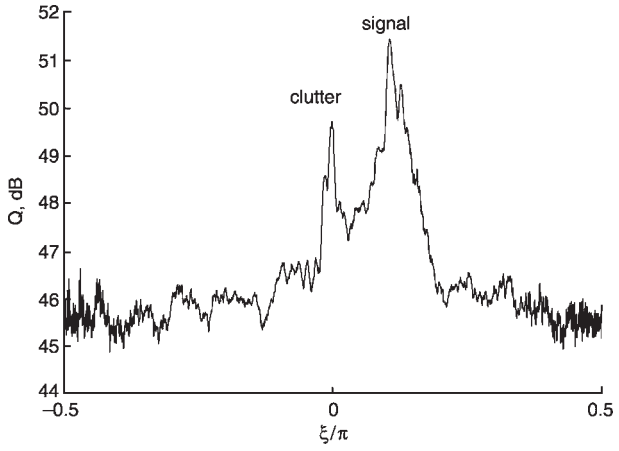

Fig. 6 *Calculated Q function (block 3)*

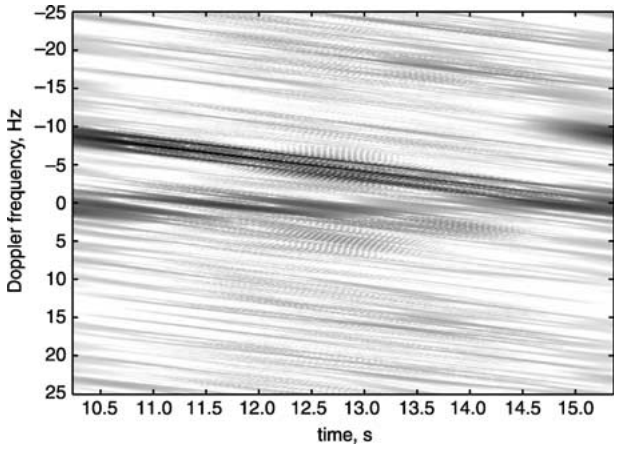

Fig. 7 *Adaptive time–Doppler distribution of the pre-whitened received signal (block 3)*

The adaptive chirp TDD is

$$C_x(t,\omega) = \frac{1}{2\pi}\sum_{\theta}\sum_{\tau} A_x(\theta,\tau)\phi_a(\theta,\tau)e^{-j\theta t - j\tau\omega} \qquad (21)$$

The above distribution has substantially suppressed clutter and noise, as well as the cross-term TDDs between the multicomponent signals. The adaptive TDD is shown in Fig. 7 for the received signal at block 3.

4.2 High-resolution time–Doppler localisation

In [14], chirp MUSIC was introduced for the estimation of the Doppler frequencies at each time index t. The estimated autocorrelation function $\hat{R}_x(t,\tau)$ is used to construct a data matrix for MUSIC spectrum estimation. However, the resulting matrix is, in general, not positive definite. Therefore, in [14], the filtered ambiguity function is transformed to the time–frequency domain, and only the positive part of the TFD is considered for the construction of the autocorrelation function. This method, although showing good time–Doppler localisation in high signal-to-noise ratio (SNR) situations, is computationally inefficient because spectrum estimation is implemented for each time index. In addition, the estimated time–Doppler signature is not always consistent with the true values, particularly in low SNR scenarios. Therefore, it is not a candidate for application in the underlying OTHR applications.

In this paper, we obtain the autocorrelation directly from the filtered ambiguity function as

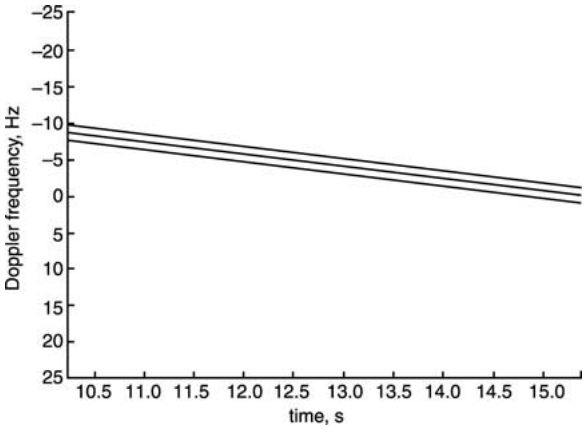

Fig. 8 *Estimated time–Doppler signature via chirp root-MUSIC algorithm (block 3)*

$$\hat{R}_x(t,\tau) = \frac{1}{2\pi}\int A_x(\theta,\tau)\phi_a(\theta,\tau)e^{-j\theta t}d\theta \qquad (22)$$

Because signal components with single chirp rate are involved, the autocorelation function $R_{x,i}(t,\tau)$ of each chirp component has the form

$$R_{x,i}(t,\tau) = A_i^2 e^{j(\alpha_i+\beta_x t)\tau} \qquad (23)$$

which is dependent on t. Such dependence can be removed by using the estimated value, $\hat{\beta}_x = -1/\tan(\hat{\xi}_x)$. From $R_{x,i}(t,\tau)$, the time-independent autocorrelation function is estimated as

$$\tilde{R}_x(\tau) = \int \hat{R}_x(t,\tau)e^{-j\hat{\beta}_x t\tau}dt \qquad (24)$$

The coherent integration yields coherent MUSIC subspace estimation of α_i for improved performance. The vector $\tilde{R}_x(\tau)$ is considered as raw data sequence, rather than as covariance elements adopted in [14], to ensure the positive definiteness of the covariance matrix for spectrum estimation. In our simulations, the root-MUSIC algorithm is used for computational convenience. Only one root-MUSIC operation is required for each block. The chirp signatures at different times are then constructed using the estimated chirp rate and α_i.

In Fig. 8, the coherent time-varying root-MUSIC spectrum is shown for block 3. Despite the low SCR, the time–Doppler signatures, along with the Doppler frequency difference information, are estimated clearly and consistently. Simulation results for all other blocks also confirmed successful Doppler signature estimation.

4.3 TDD magnitude compression and more simulation results

The existence of strong time–Doppler values at some discrete points, however, may sometimes create undesired time–Doppler signatures. Because the desired TDDs typically show much more consistent signature over all samples with its true chirp rate, we propose the use of the following magnitude compression of $C_x(t,\omega)$:

$$C'_x(t,\omega) = |C_x(t,\omega)|^{\gamma}\text{sign}[C_x(t,\omega)] \qquad (25)$$

where $0 < \gamma < 1$. Our experience suggests that γ should take value between 0.1 and 0.5. $C'_x(t,\omega)$ is used instead to estimate the autocorrelation function $\hat{R}_x(t,\tau)$ in (26).

When the TDD magnitude compression is performed, the local autocorrelation function $R_x(t,\tau)$ should be obtained from

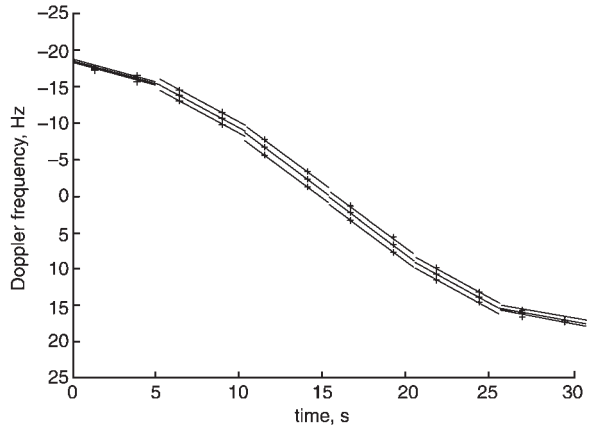

Fig. 9 *Estimated time–Doppler signature of all blocks with magnitude compression*

'+' marks show the theoretical Doppler frequencies for the three paths

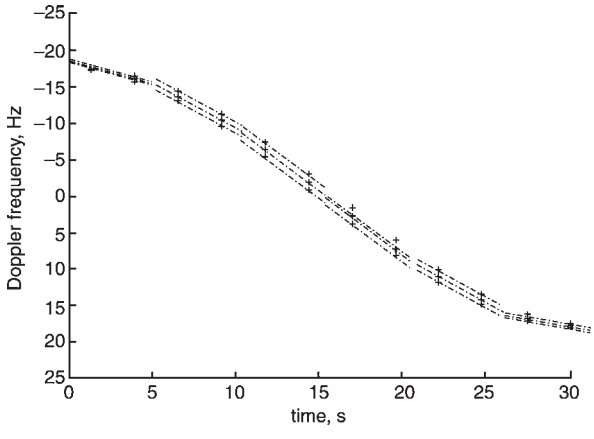

Fig. 10 *Estimated time–Doppler signature of all blocks without magnitude compression*

'+' marks show the theoretical Doppler frequencies for the three paths

$$\hat{R}_x(t,\tau) = \frac{1}{4\pi}\sum_{\omega} C'_x(t,\omega)e^{j\tau\omega} \tag{26}$$

In Fig. 9, the time–Doppler signatures obtained from the proposed method are shown for the entire turning process of the aircraft. In the computations, the results are calculated from six blocks, each of 256 samples. $\gamma = 0.2$ is used for each block. The theoretical values of the Doppler signatures are overlaid in the plot. It is evident that the proposed method provides stable and consistent estimation of the Doppler signatures over different situations.

To show the importance of applying magnitude compression, we plotted in Fig. 10 the time–Doppler signatures obtained without the magnitude compression. It is seen that, while most time–Doppler signatures are correctly estimated, one component in block 4 is not. The reason is simply that, in the process of clutter suppression, signal component with close spectrum to the clutter may lose part of its signal power.

5 Conclusions

In this paper, a novel method has been proposed for high-resolution time–Doppler signature localisation applied to over-the-horizon radar systems. By combining AR pre-whitening for effective clutter suppression, time–frequency based signal discrimination and coherent high-resolution spectrum analysis, the proposed method provides a robust estimation of time-varying Doppler signature in low signal-to-clutter ratio (SCR) scenarios.

6 Acknowledgments

This work was supported by the Office of Naval Research under Grant N00014-98-1-0176.

7 References

1 Headrick, J.M., and Skolnik, M.I.: 'Over-the-horizon radar in the HF band', *Proc. IEEE*, 1974, **62**, pp. 664–673
2 Kolosov, A.A.: 'Over-the-horizon radar' (Artech House, Boston, MA, USA, 1987)
3 McNamara, L.F.: 'The ionosphere, communications, surveillance, and direction finding' (Krieger Publishing, Malabar, FL, USA, 1991)
4 McNeal, G.D.: 'The high-frequency environment at the ROTHR Amchitka radar site', *Radio Sci.*, 1995, **30**, pp. 739–746
5 Headrick, J.M., and Thomason, J.F.: 'Naval applications of high frequency over-the-horizon radar', *Nav. Eng. J.*, 1996, **108**, pp. 353–359
6 Cohen, L.: 'Time-frequency analysis' (Prentice–Hall, Englewood Cliffs, NJ, USA, 1995)
7 Choi, H.I., and Williams, W.J.: 'Improved time-frequency representation of multicomponent signals using exponential kernels', *IEEE Trans. Acoust. Speech Signal Process.*, 1990, **37**, pp. 1132–1143
8 Jones, D.L., and Baraniuk, R.G.: 'An adaptive optimal-kernel time-frequency representation', *IEEE Trans. Signal Process.*, 1995, **43**, (10), pp. 2361–2371
9 Wang, G., Xia, X.-G., Root, B.T., Chen, V.C., Zhang, Y., and Amin, M.G.: 'Manoeuvring target detection in over-the-horizon radar by using adaptive chirplet transform with subspace clutter rejection', *IEE Proc. Radar Sonar Navig.*, 2003, **150**, (4), pp. 292–298
10 Kraut, S., Harmanci, K., and Krolik, J.: 'Space-time adaptive processing for over-the-horizon spread-Doppler clutter estimation'. Proc. IEEE Sensor Array and Multichannel Signal Processing Workshop, Cambridge, MA, USA, March 2000, pp. 245–249
11 Barnum, J.: 'Ship detection with high-resolution HF skywave radar', *IEEE J. Ocean. Eng.*, 1986, **11**, (2), pp. 196–209
12 Nohara, T.J., and Haykin, S.: 'AR-based growler detection in sea clutter', *IEEE Trans. Signal Process.*, 1993, **41**, (3), pp. 1259–1271
13 Kay, S.M.: 'Modern spectral estimation: theory and applications' (Prentice–Hall, Englewood Cliffs, NJ, 1998)
14 Mickel, R.M., and Williams, W.J.: 'High resolution frequency tracking via non-negative time-frequency distributions', Proc. IEEE Workshop on Statistical signal and array processing, Pocono, PA, USA, Aug. 2000